Influence of zirconium on cation mobilities in Na2O-CaO-Al2O3-SiO2 melts: a multicomponent diffusion and XANES study

M. Ficheux, E. Burov, L. Cormier, E. Gouillart, N. Trcera

Influence of zirconium on cation mobilities in Na_2O-CaO-Al_2O_3-SiO_2 melts: a multicomponent diffusion and XANES study

M. Ficheux[a,b], E. Burov[a], L. Cormier[b,*], E.Gouillart[a], N. Trcera[c]

[a]*Surface du Verre et Interface (UMR 125), CNRS/Saint-Gobain Research Paris, 39 quai Lucien Lefranc, 93300 Aubervilliers, France*

[b]*Sorbonne Université, CNRS UMR7590, MNHN, IRD, Institut de minéralogie, de physique des matériaux et de cosmochimie (IMPMC), 4 place Jussieu, F-75005 Paris, France*

[c]*Synchrotron SOLEIL, F-91192, Gif Sur Yvette, France*

Abstract

High temperature cation mobilities, based on the multicomponent diffusion method, have been coupled with a structural investigation in the Na_2O-CaO-Al_2O_3-SiO_2-ZrO_2 (NCASZ) system at 1200°C and 1250°C. From structural investigation using X-ray absorption spectroscopy (XANES), zirconium was determined in six-fold coordinated sites in the reduced glass composition range of our study and no significant structural changes have been evidenced compared to a quaternary Na_2O-CaO-Al_2O_3-SiO_2 (NCAS) glass with a similar composition. Additionally, the diffusion experiments revealed that adding zirconium in the quaternary melt has no influence on the dominant eigenvectors that correspond to exchange between calcium and sodium. Despite the expected mobility decrease resulting from a viscosity increase upon the addition of zirconium, the dominant eigenvalue calculated in this study is higher when Zr is introduced in the melt structure. This result strongly suggests that the sodium mobility is enhanced by the presence of Zr, which is explained by a change in the structural role of sodium from network modifier associated to Q^3(Si) sites in NCAS melts to charge compensator associated with $[ZrO_6]^{2-}$ sites in NCASZ melts. This modification generates lower bond strengths between sodium and other cations in the melt, thus favoring an enhancement in mobility. Moreover, the diffusion matrix was applied to predict diffusion profiles between zirconium-bearing crystals and melts. We observed that even far from the composition field used for the matrix determination, predictions of zirconium diffusion profiles may be relevant and demonstrate the potential of this approach to evaluate crystal/melt dissolution behavior.

*Corresponding author. Tel:. +33 1 44 27 52 39
E-mail address: laurent.cormier@sorbonne-universite.fr (L. Cormier)

1.INTRODUCTION

Zirconium is an important component in silicate glasses and melts of geological or industrial interests. In geology, zirconium has been frequently studied to understand the formation of zircon ($ZrSiO_4$), which is an important mineral in geochronological studies and in inferring paleo-formation conditions (Valley et al., 2005). The growth shape and content of radioisotopes of those crystals may be used to deduce eruption history and magma chamber residence time (Simon et al., 2008). One of the main parameters on the formation and survival of zircon is the diffusivity of Zr within silicate melts, which has been extensively investigated (Baker and Watson, 1988)(Behrens and Hahn, 2009)(Boehnke et al., 2013)(Harrison and Watson, 1983)(Mungall et al., 1999)(Zhang and Xu, 2016). Concerning industry, a major benefit to add zirconium within glass compositions is to enhance the chemical durability. Even a small amount (about 2 wt% ZrO_2) increases significantly acid and alkaline durability of a glass (Dimbleby and Turner, 1926). This chemical durability is particularly useful for long term disposal of nuclear wastes (Galoisy et al., 1999)(Gin et al., 2013) where the borosilicate-based glass containing few wt% ZrO_2 has to stand against water and alkali leaching for a very long time scale. Higher contents of ZrO_2 (about 16 wt%) are also used in commercial glass fibers for cement reinforcement where a very high alkaline durability is desired (Larner et al., 1976). Another major use of Zr is in the formation of glass-ceramics. Its structural role as nucleating agent promotes bulk crystallization of nano-phases that serve as local heterogeneities for the crystallization (Dargaud et al., 2010)(Dargaud et al., 2011). However, the ability of zirconium oxide to crystallize may also induce problems in other domains. For example, during industrial float glass production, zirconium may leave the furnace walls to enter in the melted glass (Manfredo and McNally, 1984)(Rahimi et al., 2011). Local points in the melt with high Zr concentration may crystallize (Heitz, 1999), creating defects for the final glass products.

In the aforementioned domains, phase separation and crystallization mechanisms must be mastered in order to control the properties of the melt. Unfortunately, in our knowledge no studies focusing on industrial melts are available. In rhyolitic melts, past investigations show that a zircon crystal grows until 925°C while it dissolves above this temperature (Zhang and Xu, 2016). These high-temperature mechanisms are controlled by chemical diffusion of the elements in the melt (Bouttes et al., 2015)(Chen and Zhang, 2008)(Edwards and Russell, 1996)(Mazurin and Streltsina, 1972)(Roskosz et al., 2006). Most of the time, the chemical diffusion of the slowest diffusing element drives the mechanism. Studies on Zr diffusion, based on simple Fick's law, enable to determine Zr diffusion coefficients (D_{Zr}) depending on temperature, pressure, water content, but they are only valid for the specific studied composition (LaTourrette et al., 1996)(Zhang et al., 2010). As an example, Zr diffusion in dry rhyolite melts is around 10^{-14} $m^2.s^{-1}$, while Na diffusion coefficient in same conditions can reach 10^{-9} $m^2.s^{-1}$ at 1200 °C (Zhang et al., 2010). Such studies give accurate results but are strictly limited to one specific glass/melt composition. Moreover, microscopic diffusion mechanisms remain unclear.

In order to describe the mobility of each element and be more flexible concerning the compositional field where diffusions coefficients are relevant, previous authors have studied the chemical diffusion in melts through a multicomponent approach (Claireaux et al., 2016)(Guo and Zhang, 2016)(Guo and Zhang, 2018)(Liang, 2010)(Liang et al., 1996b). This multicomponent diffusion approach describes mobility of each element considering interactions with others, allowing the description of complex diffusion phenomena like uphill diffusion (i.e., diffusion of a component in a direction opposite to its concentration gradient)

(Liang et al., 1996b). In this latter case, an initially flat concentration profile becomes a gradient generated by strong coupling with another element. The multicomponent diffusion approach takes into account interactions between elements assuming a linear model and determines a diffusion matrix which contains cross diffusion coefficients. The matrix describes the mobility of an element under its own gradient of chemical potential as driving force (diagonal terms) and the impact of the other elements on this driving force by the coupled diffusion coefficients (off-diagonal terms). The eigenvectors of the diffusion matrix give information on the coupling between species in the form of exchange reactions and eigenvalues give the occurrence coefficients of those reactions (Chakraborty et al., 1995b)(Chakraborty et al., 1995a). Several studies have been carried out at high temperatures for silicate melts in various systems: Na_2O-CaO-SiO_2 (NCS) (Trial and Spera, 1994), K_2O-Al_2O_3-SiO_2 (KAS) (Chakraborty et al., 1995b)(Chakraborty et al., 1995a)., MgO-Al_2O_3-SiO_2 (MAS) and CaO-MgO-Al_2O_3-SiO_2 (CMAS) (Kress and Ghiorso, 1993)(Richter et al., 1998), CaO-Al_2O_3-SiO_2 (CAS) (Liang et al., 1996b)(Sugawara et al., 1977) and recently Na_2O-CaO-Al_2O_3-SiO_2 (NCAS) (Claireaux et al., 2016)(Claireaux et al., 2019). Guo and Zhang investigated multicomponent diffusion in more complex systems with a 7-components haplobasalt and a 8-components basalt (Guo and Zhang, 2016)(Guo and Zhang, 2018). A recent paper focused on the ternary Na_2O-B_2O_3-SiO_2 (NBS) (Pablo et al., 2017).

In this work, we study multicomponent diffusion in NCAS melt with the addition of ZrO_2. Using the multicomponent approach, the determination of the diffusion matrix requires that no structural changes occur along a diffusion profile. However, addition of zirconium within the glass structure may result in different local Zr environments. After saturation (Kato and Araki, 1986), Zr may crystallize in ZrO_2, occurring in 7-fold coordination $^{[7]}$Zr for monoclinic/tetragonal phases and in 8-fold coordination $^{[8]}$Zr for the cubic high temperature phase (Howard et al., 1988). In NAS glass, from low concentration to saturation, Zr is usually 6-fold coordinated $^{[6]}$Zr (Cormier et al., 2015). Zr in 7-fold coordinated environment has been evidenced in CMAS glasses (Cormier et al., 2015) and minor amounts of $^{[7]}$Zr are also observed in sodo-borosilicate glasses with increasing ZrO_2 content (McKeown et al., 1999). In order to address a possible Zr coordination change with compositions in the studied glasses/melts, X-ray absorption spectroscopy is a well-suited method (Cormier et al., 2015)(McKeown, 2000)(Galoisy et al., 1999), providing high spatial resolution and enabling *in situ* measurements.

In order to prevent any crystallization, we have studied a system with a low amount of ZrO_2 (about 3 wt%). Na cations were introduced in excess of (Zr+Al) to ensure complete charge compensation of these elements, thereby limiting possible coordination changes observed for Zr (Calas et al., 2014) or Al (Neuville et al., 2006) when insufficient charge compensation is provided by alkali/alkaline earth cations.

2. EXPERIMENTAL

2.1. Sample composition and preparation

The composition domain investigated here is centered on the peralkaline composition C_0 = 62.5 wt% SiO_2, 12.9 wt% Na_2O, 10.5 wt% CaO, 10.9 wt% Al_2O_3, 3 wt% ZrO_2 (66.4SiO_2-13.3Na_2O-11.95CaO-6.8Al_2O_3-1.55ZrO_2 in mol%). This C_0 glass has a composition close to a

window glass (typically 75SiO_2-15Na_2O-10CaO), with the addition of Al_2O_3 and ZrO_2. Excess of aluminium and zirconium in industrial glass is often observed at the interface between the melt and the refractory. C_0 is also a composition similar to the NCAS glass (without ZrO_2) previously studied by Claireaux *et al.* (Claireaux et al., 2016)(Claireaux et al., 2019), allowing direct comparison to understand the influence of Zr on the diffusion properties. Around this C_0 central composition, 14 different glasses have been synthesized and compositions of the diffusion couples are summarized in Table 1. Glasses are gathered in pairs, now designated as glasses couples to create a diffusion exchange between two elements. For example, AZ glass is enriched by 2 wt% Al_2O_3 and depleted by 2 wt% ZrO_2 compared to C_0. It is coupled with ZA glass which is enriched by 2 wt% ZrO_2 and depleted by 2 wt% Al_2O_3.

Table 1. Measured composition in weight% of C_0 central composition, glass couples, $ZrSiO_4$ zircon crystal and G1 synthesized glass composition. Tg values are obtained using Fluegel's model (Fluegel, 2007). An error of ± 0.05 wt% may be considered on these values.

	C_0	AN	NA	AC	CA	NC	CN	NZ	ZN	SZ	ZS	AZ	ZA	ZC	CZ	$ZrSiO_4$	G1
Na_2O	12.9	9.5	14.2	12.7	12.1	14.4	10.3	13.3	11.4	12.2	11.9	12.3	12.4	12	13.7	0	14.4
CaO	10.5	9.8	11.1	8.6	11.4	8.47	14.8	9.9	9.1	9.9	9.6	9.4	10	9.6	12.9	0	9.9
ZrO_2	3	2.8	2.6	2.8	2.5	2.8	2.7	0.9	4.5	0.9	4.4	0.9	4.2	4.4	1.1	67	0
Al_2O_3	10.9	14.1	9.5	13.2	9.5	11.6	11.7	11.4	11.4	11.0	11.4	12.7	9.2	11.5	11.5	0	0.6
SiO_2	62.5	63.7	62.5	64.2	65.2	61.3	60.1	63.3	63.7	65.4	62.1	61.5	61.2	62.5	61.3	33	75
Tg	612	654	597	623	612	602	638	603	633	609	629	616	615	629	602		

Viscosities of each glass were measured from 1100°C to 1600°C, using a high temperature Couette rheometer (Fig. S1 in the Supplementary file). The glass transition temperatures Tg were estimated using Fluegel's model (Fluegel, 2007) and reported in Table 1. The values are close to those reported in a similar system without ZrO_2 (Claireaux et al., 2019). Tg values vary around the C_0 composition and increase by about +40°C for the Al_2O_3 and ZrO_2 rich compositions, and decrease by about -20°C for the glasses with more Na_2O content and less Al_2O_3 and ZrO_2 content. However, the deviations of the Tg values are low compared to the experimental uncertainties and their influence on the diffusion processes is weak.

After diffusion through thermal treatment, this method allows us to investigate only one exchange per profile. A maximum of 4 wt% concentration difference has been chosen in order to keep the mass conservation assumption and a constant diffusion matrix through the diffusion profiles, in accordance with Fick's second law. Glasses have been synthesized using the following raw materials: Ronceveaux sand (SiO_2 > 99.7 wt%), Saint-Germain Limestone ($CaCO_3$ > 99.8 wt%), sodium carbonate from Novacarb (Na_2CO_3 > 99.9 wt%), calcined alumina (Al_2O_3 > 99.9 wt%) from Keraglass and zirconia (ZrO_2 > 99.9 wt%) from Zirpro. Some ppms of coke have also been introduced in order to improve glass homogeneity. For each couple, one of the two glasses is colored in blue by adding 200 ppm of cobalt oxide (that is the range of impurity content of used raw materials) for several reasons: the interface between two glasses (one doped with Co and the other one undoped) is easily found optically and any macroscopic convection occurring at high temperature between the two glasses is immediately observed. Glasses have been melted in a platinum crucible at 1550°C for 8h, mechanically agitated for homogeneity every hour and finally poured on a metallic table. An annealing step of 50 min at 20°C above Tg has been carried out to relieve residual internal stresses, which allows the glass to stand against various mechanical solicitation for sample sizing before diffusion experiment.

2.2. Diffusion experiments

Two temperatures have been selected: 1200°C and 1250°C. They are as close as possible to the temperature of interest for industrial and geological issues; these are also temperatures at which experiments are feasible, avoiding convection and nucleation phenomena. The risk of formation of convection cells can be estimated, in accordance with the Rayleigh number Ra defined as:

$$Ra = \frac{g.\Delta T.l^3\beta}{\frac{\eta}{d}.\alpha} \quad (1)$$

where g is the constant of gravity, ΔT the temperature variation in sample, l^3 the sample volume, β the thermal dilatation of the melted glass, η the dynamic viscosity, d the density and α its thermal diffusivity. When Ra is higher than 1700-2000, a convection cell is expected to appear. In order to avoid convections, Ra can be lowered by reducing the sample size l^3. Cylinder-shaped glass samples were used with 8 mm diameter and 4mm height (Fig. 1). The contact face of each cylinder is mechanically polished until surface asperity sizes are below 5 µm, avoiding significant bubble trapping that disturbs diffusion. The glasses couple is piled in an alumina crucible with 8 mm inner diameter, 2 mm thickness and 15 mm height (Fig. 1).

For each couple, the denser glass is placed at the bottom of the crucible in order to limit convection. Additionally, considering that alumina diffuses at high temperature from the crucible to the glass, we have not considered data that are close to the alumina crucible.

The choice of diffusion times results from a trade-off between two contradicting conditions. A long diffusion profile is needed to acquire enough points that will give an accurate spatial resolution to follow chemical composition variations along the concentration profile while, in order to avoid the apparition of convection cells, the diffusion time has to be limited. The crucibles containing samples are introduced in a preheated electric furnace then removed after 20 min. Samples are finally annealed in another furnace preheated at 10°C above Tg during 50 min. The furnace is then turned off and the samples are slowly cooled down to room temperature. Table S1 in the supplementary file summarizes the couples that were measured and the experimental conditions.

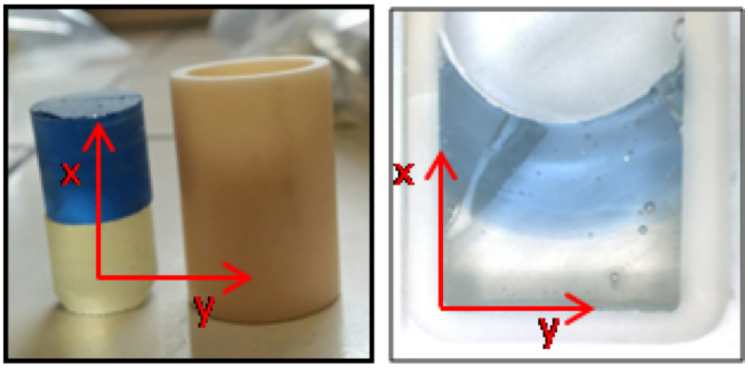

Fig. 1. Sample before heat treatment and ready for microprobe analysis.

2.3. Chemical diffusion profiles

The chemical concentration profiles of the diffusion couple samples were determined by Electron Probe Micro-Analysis (EPMA) using a Cameca SX-Five electron microprobe at the CAMPARIS center (Sorbonne University, Paris) and at Saint-Gobain Research Paris. The operating conditions were 15 kV accelerating voltage, 10 nA beam current and only 5 s counting time in order to limit the migration of light elements such as Na during acquisition. After encapsulation in epoxy resin, samples are cut and polished to 1 µm by using a series of diamond pastes. Optical microscopy was used to check that no convection cells appeared. To avoid any Na migration under the beam, the beam area has been defocussed to 5 μm^2, which reduces the received energy per μm^2. The microprobe beam was stopped during focalization before each measurement, which limits the exposition time. It was also necessary to start each new acquisition point with Na as the first analyzed element. This procedure minimizes the exposition time of the analyzed surface before collecting Na data and allows a standard deviation of Na of 0.1 wt%. Considering that this is the order of magnitude of composition inhomogeneities that we might find in our glass, we are satisfied with such accuracy.

In theory, only (n-1) experiments with (n-1) profiles are required to determine the $(n-1)^2$ coefficients of the diffusion matrix. In our case, only 4 experiments should be necessary.

However, we experimentally had reproducibility problems in the diffusion coefficients of the matrix with this limited number of profiles. We then reached an experimental setup with 7 profiles that solved our problems and gives a good reproducibility in the results. It was especially necessary to increase the number of acquired data in the exchange profile between slowly diffusing elements, such as Al, Si, Zr.

2.4. Structural profiles

The Zr $L_{2,3}$ edges are due to transition from 2p to 4d states. In Oh symmetry, the two peaks in the Zr L_2 and L_3 edges are associated with the crystal field splitting of the 4d states into t_{2g} and e_g empty states. The filling of these empty states change their energy position, which can be measured through XANES (X-ray Absorption Near Edge Spectroscopy). The XANES data at the Zr $L_{2,3}$-edges were acquired at the SOLEIL synchrotron source on the LUCIA beamline (Saint-Aubin, France) using a Si(111) double crystal monochromator. Data were recorded in fluorescence mode at ambient conditions (T = 22°C) using a silicon drift diode detector. Each spectrum is the average of at least two spectra with an energy step of 0.1 eV at a counting time of 3 seconds. After normalization of the high energy side using Athena software (Ravel and Newville, 2005), a residual background was subtracted by fitting an arctangent function. The background-free spectra have then been fitted with pseudo-Voigt functions. The parameters of the pseudo-Voigt functions give information on the 4d energy level that are related to the coordination number. XANES spectra were obtained for crystalline references containing Zr in different environments: Baghdadite ($Ca_3ZrSi_2O_9$) with Zr coordination number N = 6 ($^{[6]}$Zr), Baddeleyite (monoclinic ZrO_2) with N = 7 ($^{[7]}$Zr) and zircon ($ZrSiO_4$) with N = 8 ($^{[8]}$Zr). Using a spot size area of ~10 µm^2, XANES spectra were acquired through several diffusion profiles, with a position accuracy of ~1 µm.

Raman spectroscopy was also used to determine the average changes in network connectivity induced by the different chemical exchanges. Raman spectra were acquired using a Renishaw Qontor machine and a green laser with a wavelength of 532 nm and a power of 50 mW. The spot was focused with x50 lens and the acquisition time per spectra was 1 s. The excited zone is about 5 µm², which is comparable with EPMA. Principal Component Analysis (PCA) treatment was performed thanks to the constructor software. The temperature and frequency dependencies were corrected using the Long correction (Long, 1977) and normalized using the total area under the spectrum. The Raman spectra have been acquired along each concentration profiles. We have carefully acquired Raman spectra along the EPMA profiles in order to correlate each spectrum with its associated composition. Thereby, we can couple both composition and structural information along the same diffusion profile.

2.5. Mathematical analysis of diffusion profiles

The cooperative nature of species mobility in a multicomponent system has been analyzed using a matrix diffusion approach where eigenvectors describe coupling between species. Details about the theoretical background of the matrix approach has been discussed by Liang (Liang, 2010). The numerical procedure to determine diffusion coefficients from diffusion-couple experiments, taken as the eigenvalues of the diffusion matrix, can be found in Claireaux *et al*. (Claireaux et al., 2016).

Firstly, for each temperature, the diffusion matrix was obtained from the least-square minimization of the difference between all available experimental diffusion profiles and the theoretical diffusion profiles given by:

$$\tilde{C}_i(x,t) = \Delta\tilde{C}_i erf\left(\frac{x}{\sqrt{2\alpha_i t}}\right) \quad (2)$$

where α_i is an eigenvalue of the diffusion matrix, $\Delta\tilde{C}_i$ is the initial concentration step in the eigen-basis and $\tilde{C}_i(x,t)$ is the projection of the concentration profiles of the different species, along the direction of the eigen-vector *i.*

Secondly, we fitted the diffusion profiles at two temperatures using a common basis of eigenvectors. As discussed in Claireaux *et al*. (Claireaux et al., 2019), since the estimated direction of eigenvectors does not change much with temperature, the obtained set of eigenvalues is likely to be more accurate.

The least-square error was computed in the eigenbasis of the diffusion matrix, using the open-source code *multidiff* (https://pythonhosted.org/multidiff/).

3. EXPERIMENTAL RESULTS

The seven concentration profiles obtained at 1200°C and 1250°C are given in Fig. 2 and Fig. 3, respectively. The interface composition C_i of each diffusion couple is listed in Table S2 in the supplementary file. The diffusion distance is normalized by $\sqrt{t}$ in order to make our results independent of time. Each concentration profile is plotted relatively to the central composition C_0 for better readability ($x/\sqrt{t}$ = 0 and concentrations = 0). In a concentration profile, the two glass compositions should differ for the two elements that are added or removed compared to the composition C_0. However, small variations for other components are sometimes observed compared to the target composition (Table. 1). Most of these variations concern SiO_2 concentration, causing a small variation compared to the total SiO_2 content. These variations imply concentration gradients that can create interactions between elements during diffusion. To avoid this problem, all profiles are fitted altogether and the real concentration differences are taking into account.

Diffusion profiles are very similar at 1200°C (Fig. 2) and 1250°C (Fig. 3). As previously observed (Claireaux et al., 2016)(Guo and Zhang, 2016)(Guo and Zhang, 2018)(Liang, 2010), the exchanges between Na and Ca are much more extended in space than other ones. Na is the most mobile element and its diffusion distance does not seem to be highly impacted by the element it is exchanged with. As Na cations do not have network forming role in the melt structure, they are able to move freely within the silicate framework. The second fastest diffusing element is Ca. Its diffusion distance strongly depends on the element it is exchanged with, from very fast exchange with Na to very slow with Zr or Al. The very well-known uphill diffusion of Ca under Na/Al exchange (Liang et al., 1996a)(Zhang et al., 1989) is observed also in our system for both temperatures. An interesting point is the apparition of the same Ca strong uphill diffusion when Zr is exchanged with Na (Fig. 2,3 ZN|NZ). This uphill diffusion comes from a different mobility of Na compared to Al and Zr. From structural considerations, an exchange between two network modifiers is easier than between element with different structural roles (network modifier vs network former). This aspect will be detailed in the discussion part.

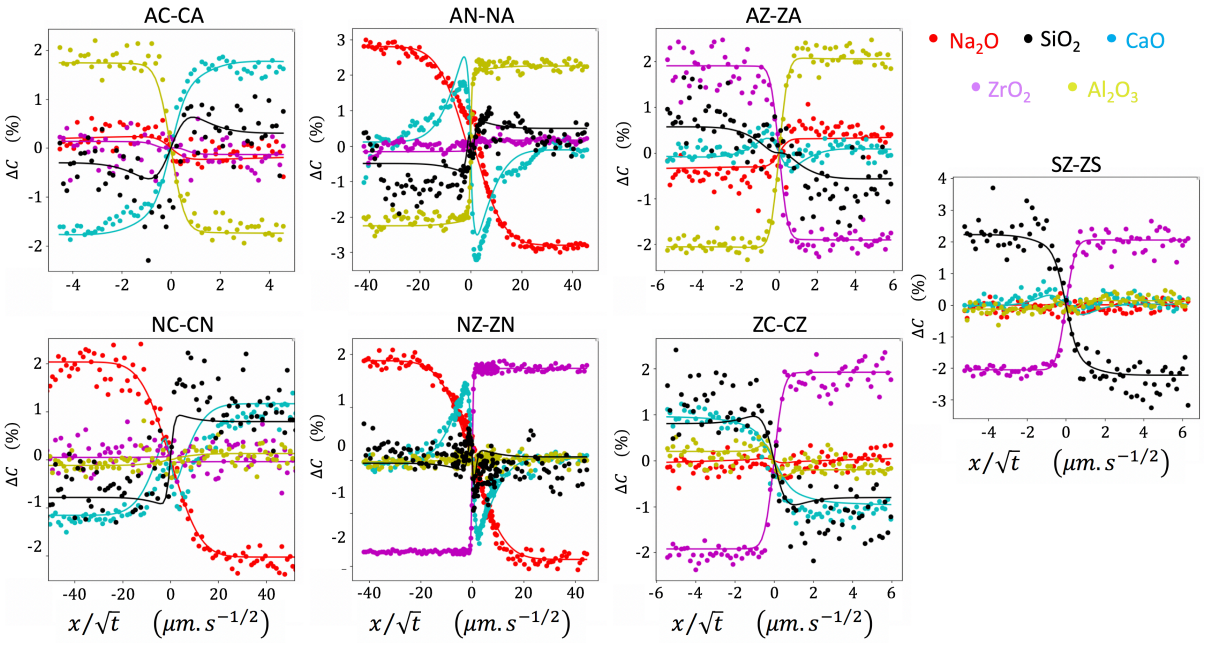

Fig. 2. Concentration profiles for all diffusion couples at 1200°C. The dots correspond to measurement when the solid lines correspond to the fit for diffusion matrix determination.

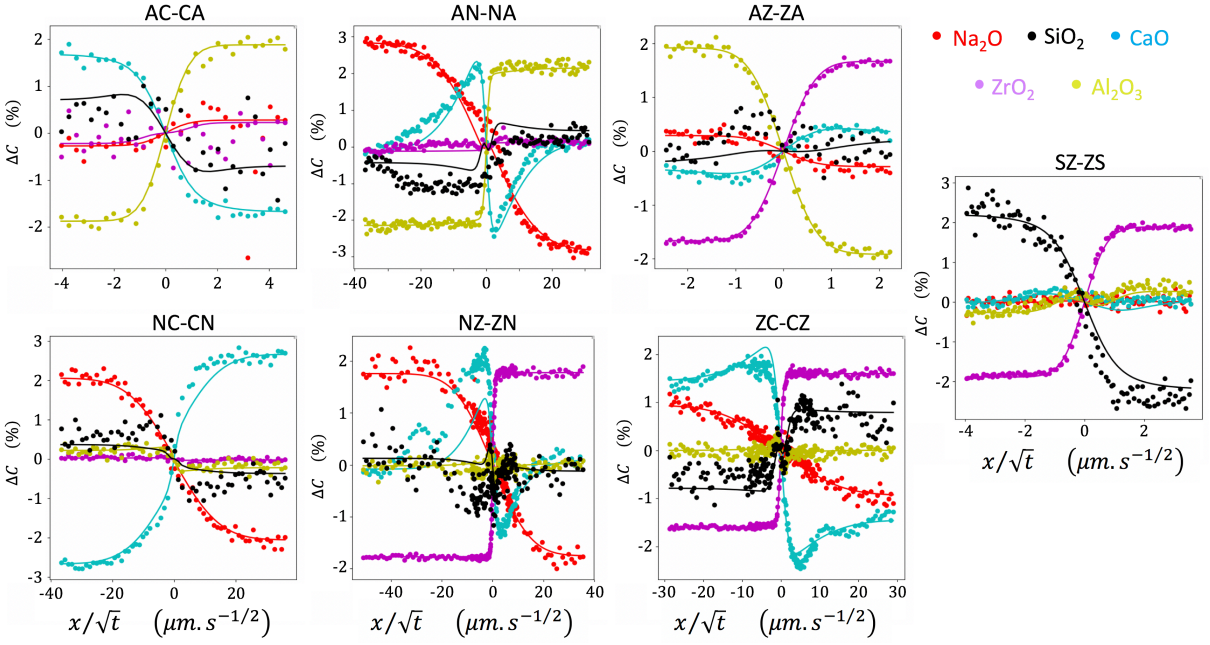

Fig. 3. Concentration profiles for all diffusion couples at 1250°C. The dots correspond to measurement when the solid lines correspond to the fit for diffusion matrix determination.

3.1 Eigenvectors and eigenvalues

The theoretical diffusion profiles obtained with the best-fit diffusion matrix correspond to the solid lines plotted behind experimental data in Fig. 2 and Fig. 3. The agreement between

experimental and theoretical profiles is very good. However, the Ca uphill profile is not well described when it is asymmetric. The eigenvectors and eigenvalues calculated for the diffusion matrix allow us to determine exchange reactions. The eigenvectors give the stoichiometry of the reaction and indicate exchange diffusion mechanisms (Guo and Zhang, 2016)(Guo and Zhang, 2018). Their associated eigenvalues indicate the rate of these reactions (Chakraborty et al., 1995b)(Chakraborty et al., 1995a). In order to obtain those eigenvectors and eigenvalues, the fit of each profile has been set up through different steps. We first proceed calculations for each temperature, independently. The obtained diffusion matrix for 1200°C and 1250°C with SiO_2 as a dependent component is given in Table 2 and the eigenvalues and eigenvectors are reported in Table 3. Those eigenvectors are expressed in wt% eigenbasis. It has already been observed that eigenvectors are almost constant with temperature (Chakraborty et al., 1995a)(Kress and Ghiorso, 1993)(Mungall et al., 1998). Our calculations confirm this result with very small changes occurring for the eigenvectors. Then, the fit of all profiles for the two temperatures was performed in a common basis of eigenvectors. The eigenvectors and the eigenvalues are given in Table 4 and compared with the results previously obtained on a similar NCAS glass without ZrO_2 (Claireaux et al., 2016). We observe that the major exchange direction is the Na/Ca exchange. The second eigenvector corresponds to Ca exchanging with network formers. The 3rd and 4th reactions are more complex and will be developed in the discussion part. Concerning the eigenvalues, their evolution follow common sense with increasing values between 1200°C and 1250°C reflecting the enhanced diffusion at higher temperatures.

3.2 XANES Spectroscopy

The Zr L_3 edge XANES spectra are plotted in Fig. 4.a for crystalline references containing $^{[6]}$Zr, $^{[7]}$Zr and $^{[8]}$Zr, showing a strong influence of the Zr coordination number and the site geometry (Bouvier et al., 2001)(Howard et al., 1988)(Wyckoff, 1963). In baghdadite, Zr occurs in a slightly distorted octahedron ZrO_6 and the spectrum presents two well-resolved peaks. In baddeleyite and zircon, the two components are poorly resolved due to the low site symmetry for $^{[7]}$Zr and $^{[8]}$Zr sites.

XANES spectra have been measured along four diffusion profiles corresponding to the couple exchanges NZ/ZN, ZC/CZ, AZ/ZA, that all include a zirconium concentration gradient, and the couple exchange AN/NA to assess possible interactions between Zr, Al and Na. The apparent crystal field splitting and relative intensities indicate that Zr is mostly in an octahedral symmetry in all glasses and along all diffusion profiles. As the changes occurring in spectra are limited along a profile, we only plot the spectra of all glass couples in Fig. 4.b. Each spectrum was fitted using two pseudo-voigt functions in order to determine the evolutions of the energy positions and full widths at half maximum (FWHM) for both peaks. No change is observed in the energy position (not shown) but the FWHM is slightly changed along several profiles (Fig. 5). It is especially clear on the NZ/ZN and AN/NA diffusion couples (Fig. 5.a and Fig 5.b). The width of the peaks increases with increasing Zr or Al content and decreases with increasing Na content. It has been recognized that charge compensation of Zr and Al sites is preferentially achieved by Na rather than Ca (Angeli et al., 2010)(Cormier et al., 2000)(Quintas et al., 2009)(Quintas et al., 2017). The narrower peaks imply better defined Zr-sites that are present when more Na atoms are available. This probably results for a better charge compensation of Zr sites that are less distorted. Conversely, when the number of Al or Zr

atoms increase, a small Zr site deformation is observed, resulting from the competition between Al and Zr for charge compensation by Na.

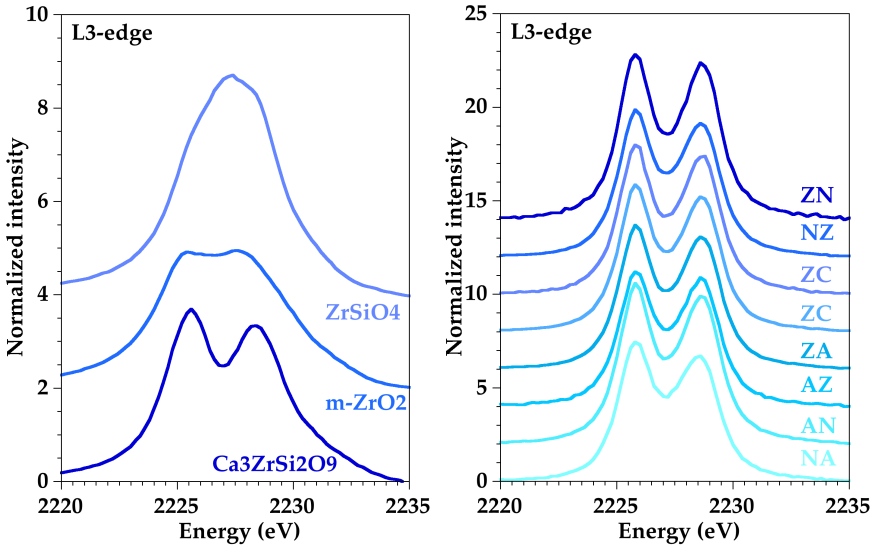

Fig. 4. Left: L_3 edge XANES references. Right: L_3 edge XANES spectra for studied coupled glass.

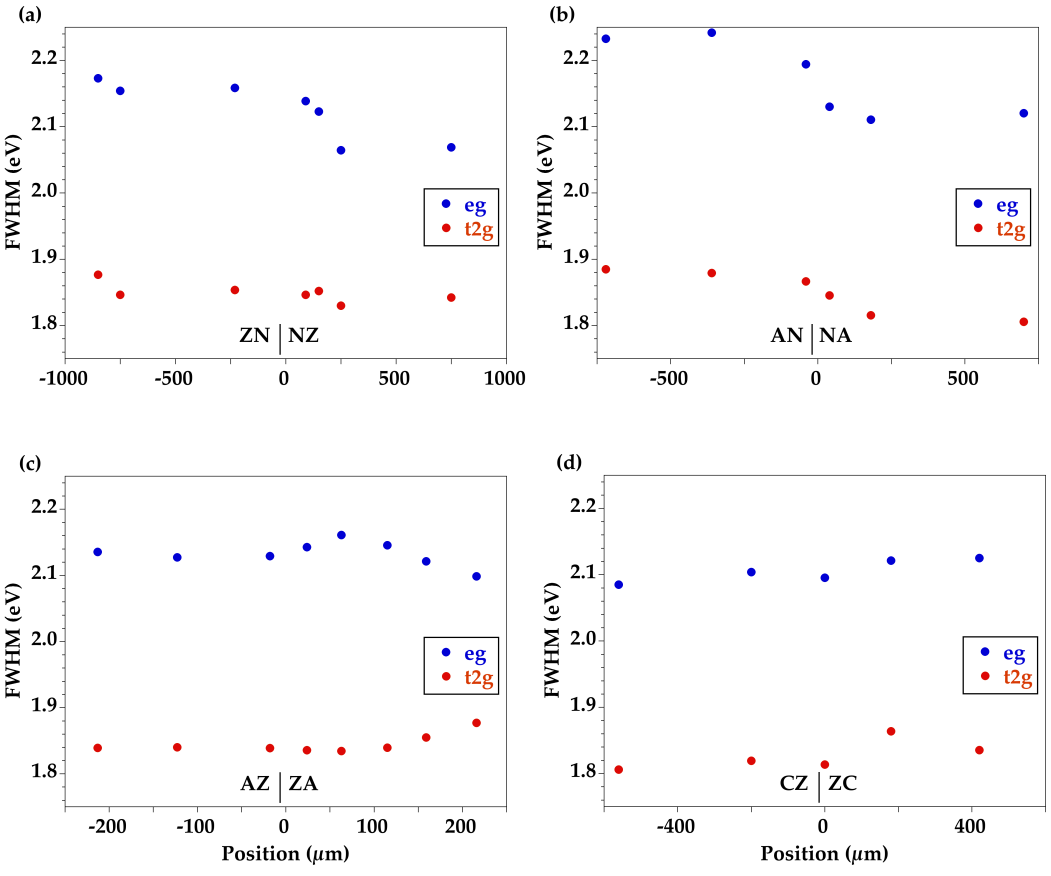

Fig. 5. Width at the middle height of Zr L_3-edge XANES profiles, corresponding to Zr site deformation through t_{2g} (first peak) and e_g (second peak) energy position.

3.3 Raman spectroscopy

Raman spectra profiles were acquired on each diffusion profile and each glass couple endmember after diffusion during 20 min at 1250°C (Fig .6). In order to detect small variations along profiles, the Raman spectra have been plotted as measured intensity (color scale) for each wavenumbers (x axis) depending on position along the diffusion profile (y axis). These plots allow a comparison of the structural changes depending on the concentration profile. We can follow the modifications through recognition of some well-known Raman vibration bands according to literature. The position of these bands is given upon and below each colormap.

On the NC/CN profile (Fig. 6.a), when Ca content increases and Na content decreases, the band at 1100 cm^{-1}, usually related to Q^3 units (with Q^n corresponding to SiO_4 species with *n* bridging oxygens), decreases in intensity and the one at 980 cm^{-1}, usually related to Q^2 units, increases in intensity (Schaller, 1999). These changes indicate a network depolymerization due to the introduction of Ca within the alumino-silicate network.

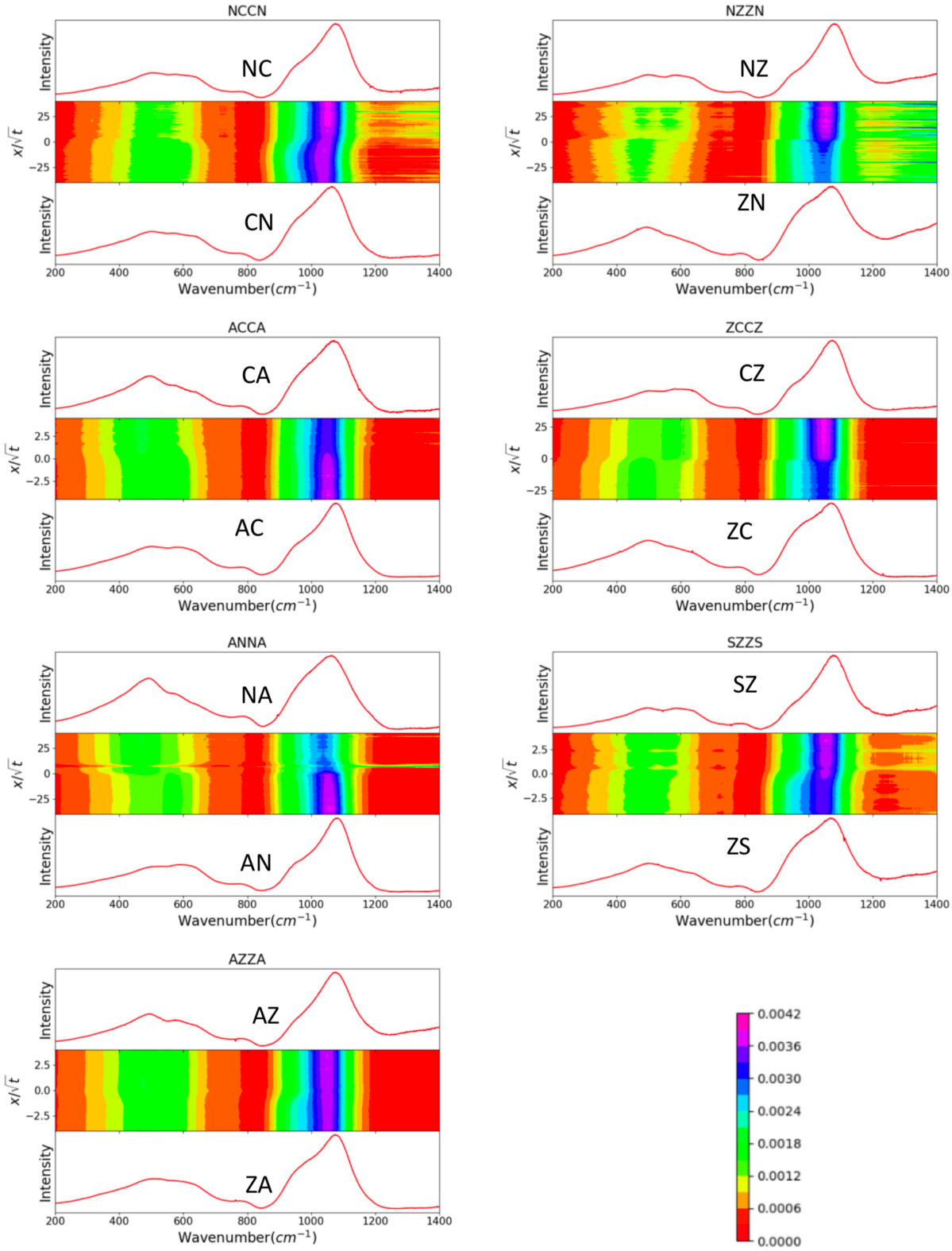

385

386 Fig. 6. Raman spectra intensity profiles acquired along diffusion profiles. Spectra of coupled
387 glass before diffusion are also plotted upon and above color map.

388

The structural modification due to Al exchange with a non-network former cation can be followed with the exchange AC/CA and AN/NA (Fig. 6.c and Fig. 6.e), respectively. In both cases, the Q^3 unit band (1100 cm^{-1}) intensity increases with Al content that indicates an increase in network connectivity. The Raman band in the 400-800 cm^{-1} region are usually attributed to inter-tetrahedral T-O-T linkages (with T = Si/Al) (McMillan and Piriou, 1982)(Mysen et al., 1982)(Neuville et al., 2004)(Petrescu et al., 2012). The aluminum exchange with both Ca and Na significantly impacts this region. The intensity of the band at 480 cm^{-1} that corresponds to Si-O-Si bending (Petrescu et al., 2012) decreases when Al content increases. At the same time, the intensity of the band at 570 cm^{-1} increases and this band is attributed to the presence of Al-O-Al bridges (Neuville et al., 2006). Similar structural evolutions with compositions in aluminosilicates glasses have been previously reported and no major changes are observed due to the presence of 3 wt% ZrO_2.

Other profiles involving Zr exchange show common specific changes (Fig 6.b, d, f, g). We first detect a band appearing at 980 cm^{-1} with increasing Zr content. Such a band has been observed in Zr-bearing glasses and it is attributed to Zr-O-Si stretching vibrations (Angeli et al., 2010). Some authors proposed that the Zr site is linked to Q^3(Si) units in borosilicates (Quintas et al., 2017). At the same time, for ZN/NZ (Fig. 6.b), ZC/CZ (Fig. 6.d) and SZ/ZS (Fig. 6.f) exchange couples, the band at 1100 cm^{-1} attributed to Q^3(Si) linked with Na decreases in intensity with Zr content. In these exchanges, we expect that Zr diffusion is associated with a structural change as Q^3(Si)-Na is replaced by Q^3(Si) linked with Zr polyhedra. This structural reorganization implies a repolymerization of the alumino-silicate network. On the contrary, when zirconium is exchanged with aluminum (Fig 6.g), we do not observe any changes on the Q^3(Si) band. This seems to indicate that Zr and Al have a similar role in the glass structure. This conclusion is in agreement with our XANES results. The increase of the characteristic band of Al-O-Al at 570 cm^{-1} is also observed when Al content increases.

4. DISCUSSION

4.1. Influence of zirconium on mobility in NCASZ glass

In order to rationalize the effect of Zr on chemical mobility in NCASZ glass, discussion will be based on a comparison of our results with previous ones obtained in the NCAS system with similar compositions. Considering the eigenvectors determined in NCAS and NCASZ (Table 4), addition of ZrO_2 does not strongly modify the two main eigenvectors that are V_1 and V_2. Indeed, influence of zirconium is weak and more related to minor eigenvectors such as V_3 and V_4. The eigenvalues of NCASZ are roughly 262 times lower for V_3 compared to V_1. The observation of the same eigenvectors for NCAS and NCASZ glasses allows a comparison of the eigenvalues for the two systems for different temperatures (Fig. 7). At the same temperature (1200°C), the eigenvalues corresponding to the first and second eigenvectors are higher by ~1.6 factor for V_1 and 1.84 factor for V_2 when 3 wt% ZrO_2 is added, which indicates that diffusion along these eigenvectors is accelerated by the addition of ZrO_2. As far as we know, this phenomenon has not been observed previously. However, a recently published study (Zhang et al., 2018) showed that a small amount of ZrO_2 in $2SiO_2$-Na_2O binary glasses increases Na mobility in terms of ionic conductivity in the temperature range of 200-400°C. Our present study could reflect the same phenomenon with chemical potentials and not electrical

potentials as driving forces. This result is counterintuitive if we consider diffusivity related to viscosity variation as stated in the Eyring model (Eyring, 1936):

$$D^E = \frac{k_B T}{\eta d} \quad (3)$$

where η is the melt viscosity, and *d* is a typical jump distance corresponding to a diffusive step. *d* is usually taken as the oxygen-oxygen interatomic distance d = 2.8 Å (Lesher, 2010)(Ni et al., 2015)(Zhang et al., 2010). Concerning η, we used the measured viscosity values for NCAS (Claireaux et al., 2016), and our own measured viscosity data for NCASZ (Fig. S1 in the Supplementary file). As expected, due to the large bond strength of the Zr-O bond, addition of ZrO_2 increases viscosity. The diffusion coefficients derived from Eq. 3 (Fig. 8) match self-diffusivities of network formers in high temperature melts (Zhang et al., 2010). The solid lines are the Eyring diffusion coefficients for NCAS endmembers while the dotted lines represent the diffusion coefficients for the same NCAS with 3 wt% ZrO_2. We observe (Fig. 8) that adding ZrO_2 decreases Eyring diffusivities of all network formers. For example the AN value of diffusivity is always higher than the AN_{Zr} value of the same glass with ZrO_2. In conclusion, if diffusion is ruled by viscosity only, the diffusivity should decrease as ZrO_2 content increases.

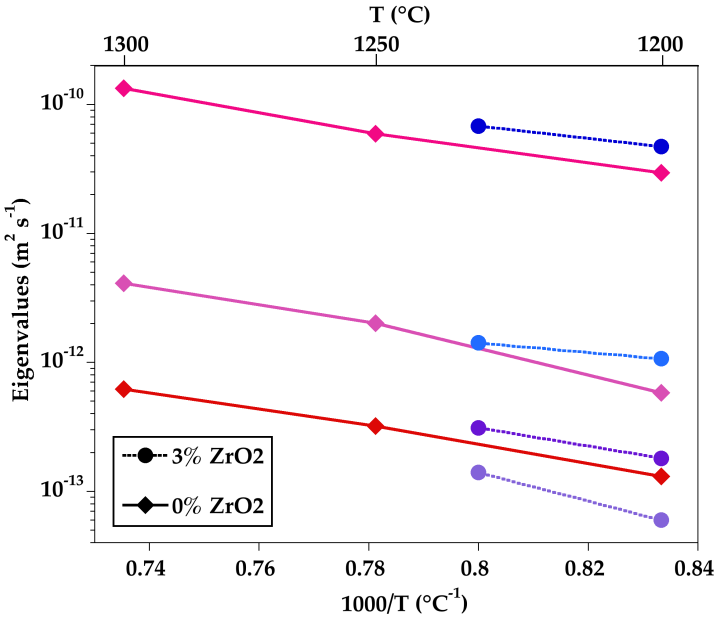

Fig. 7. Eigenvalues obtained for diffusion matrix and corresponding to the exchange reactions. The dotted lines with circles are the eigenvalues of this study when the triangles correspond to the values in Claireaux et al. (Claireaux et al., 2016, 2019) for higher temperatures.

In order to understand this contradiction that diffusivity of some elements increase with viscosity, we correlate structural changes with diffusion paths. To this purpose, the eigenvectors (Table 4) can be interpreted as exchange reactions between ions (Chakraborty et al., 1995a) and we convert weight concentration in Table 4 to mole concentration in the following equations. This conversion results in the following reactions:

$$V_1 = 1.1CaO \leftrightarrow 0.95Na_2O \quad (4)$$

$$V_2 = 1.1CaO \leftrightarrow 0.8SiO_2 + 0.1Al_2O_3 \quad (5)$$

$$V_3 = 0.9\,SiO_2 + 0.7CaO \leftrightarrow 0.65Al_2O_3 + 0.2ZrO_2 + 0.15Na_2O \quad (6)$$

$$V_4 = 0.5\,ZrO_2 + 0.3CaO \leftrightarrow 0.6Al_2O_3 + 0.2SiO_2 + 0.15Na_2O \quad (7)$$

The first reaction (Eq. 4) can be easily interpreted as an exchange of non-network formers in the melt structure. This exchange was observed repeatedly in previous studies (Claireaux et al., 2016)(Trial and Spera, 1994). This reaction has also the highest eigenvalue, indicating that it is the fastest homogeneous melt reaction. This is consistent with the high mobility of alkalis and alkaline earths in melts compared to network formers (Si, Al and Zr in the present case).

Table 2. Diffusion matrix obtained separately for temperatures at 1200°C and 1250°C with SiO_2 as dependent component. Coefficient are given in $10^{-12}m^2.s^{-1}$. Errors on the values are less than 5% (Claireaux et al., 2019).

	1200°C				**1250°C**			
	Na_2O	**CaO**	**ZrO_2**	**$Al2O_3$**	**Na_2O**	**CaO**	**ZrO_2**	**$Al2O_3$**
Na_2O	45.35	-0.52	0.02	-6.85	65.57	-0.75	0.04	-9.87
CaO	-48.44	1.69	0.24	7.89	-67.03	2.24	2.39	1.12
ZrO_2	-0.63	-0.09	0.04	0.05	-0.88	-0.10	0.14	0.11
Al_2O_3	-1.36	-0.12	0	0.22	-1.9	-0.13	0.07	0.47

Table 3. Eigenvectors and eigenvalues ($10^{-12}m^2.s^{-1}$) obtained by fitting experimental data separately for temperatures at 1200°C and 1250°C in independent eigenbasis.

	NCASZ – 1200°C				**NCASZ – 1250°C**			
	V1	V2	V3	V4	V1	V2	V3	V4
Na_2O	-0.97	-0.06	0.18	-0.15	-0.82	-0.04	0.08	-0.06
CaO	1	1	-0.59	0.13	1	1	-0.71	0.22
ZrO_2	0.02	-0.03	0.09	1	-0.02	0.10	0.45	1
Al_2O_3	0.05	-0.15	1	-0.78	-0.01	-0.17	1	-0.69
SiO_2	-0.1	-0.75	-0.68	-0.19	-0.17	-0.76	-0.83	-0.46
α^{1200}	38.2	0.83	0.12	0.06				
α^{1250}					65.41	1.39	0.32	0.13

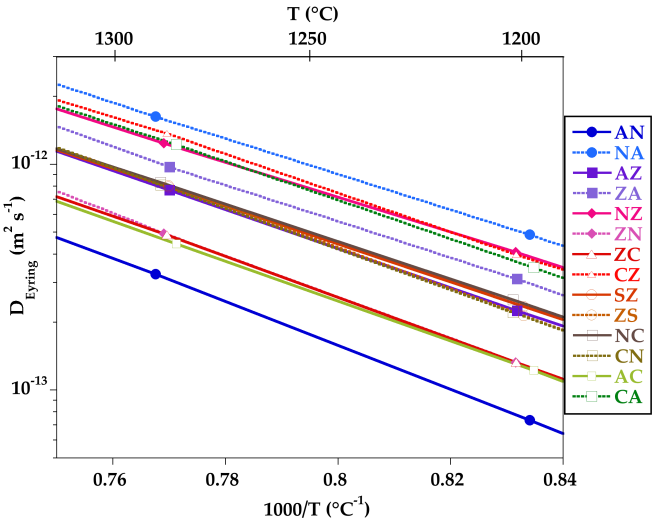

Fig. 8. Eyring diffusivity for different NCASZ endmembers with ZrO_2 (dash line) and without ZrO_2 (solid line).

Table 4. Eigenvectors and eigenvalues ($10^{-12}m^2.s^{-1}$) obtained by fitting experimental data for 1200°C and 1250°C in common eigenbasis for NCASZ and given by Claireaux et al.(Claireaux et al., 2016) for NCAS.

	NCASZ				NCAS		
	V1	V2	V3	V4	V1	V2	V3
Na_2O	-0.96	0.06	0.14	-0.14	1	0.02	-0.15
CaO	1	1	-0.69	0.25	-0.92	1	0.98
ZrO_2	0.00	-0.02	0.39	1	X	X	X
Al_2O_3	0.05	-0.15	1	-0.96	0.02	-0.47	-1
SiO_2	-0.09	-0.89	-0.84	-0.14	-0.09	-0.52	0.17
α^{1200}	47.20	1.07	0.18	0.06	29.5	0.58	0.13
α^{1250}	67.69	1.42	0.31	0.14			
α^{1280}					59.1	2.01	0.32
α^{1360}					133	4.1	0.62

The second reaction (Eq. 5) is an exchange between a non-network former (Ca) and network formers (Si and Al). The same reaction has been evidenced in CAS (Liang et al., 1996a) and NCAS (Claireaux et al., 2016) but with different stoichiometric numbers for Al and Si. Addition of Zr in NCAS tends to increase the number of Si exchanged with Ca. The corresponding eigenvalue is also higher in NCASZ compared to NCAS.

The third reaction (Eq. 6) describes the exchange of alumina for silica which is accompanied by an associated flux of Na and Ca cations. This reaction was also observed in the NCAS system (Claireaux et al., 2016). However, the corresponding stoichiometric numbers are different and, in the present case, there is also a minor amount of Zr that is involved in the

exchange for Si and Ca. The fourth reaction (Eq. 7) is the major reaction involving Zr. It corresponds to the exchange of Zr for Al and a minor Si amount, with again including Ca and Na cations. Furthermore, it has the smallest eigenvalue and highest incertitude. Thereby, there is a minor influence of this exchange on the overall diffusion processes.

If now we consider the observed structural behavior of each element in the melt structure along the diffusion profile, we can better understand the propensity of Zr to accelerate Na mobility in the reaction V_1. Indeed $[ZrO_6]^{2-}$ octahedra preferentially need to be charge compensated by nearby Na^+ atoms (Angeli et al., 2010)(Cormier et al., 2000)(Quintas et al., 2017). According to Raman spectra along diffusion profiles (Fig 6), the number of Q^3(Si) decreases when ZrO_2 is exchanged with SiO_2 (Fig 6.f). Consequently, as a ZrO_6 octahedra is formed, two Na^+ cations initially close to a non-bridging oxygen belonging to a Q^3 species (role of network modifier) move near a Zr atom to ensure charge compensation of the $[ZrO_6]^{2-}$ site. The overall behavior can be described as:

$$[ZrO_6]^{2-} + 2Na^+(charge\ compensator) \leftrightarrow 2Q^3(Si) + 2Na^+(network\ modifier) \quad (8).$$

To our knowledge, no data exist on Na-O bond lengths when Na is charge compensating $[ZrO_6]^{2-}$. However, concerning other negatively charged polyhedra ($[AlO_4]^-$, $[BO_4]^-$), the Na-O distance is generally larger when Na is charge compensator rather than network modifier (Angeli et al., 2010). The electrostatic binding energy of alkali being inversely proportional to the Na-O distance (Greaves and Ngai, 1995), a shorter Na-O distance implies a deeper depth of the Coulomb well and important trapping of alkalis that consequently reduces their mobility. Indeed, the negative charge that Na^+ cations compensate as a network modifier is spatially localized for a NBO on a Q^n species and more delocalized for a $[ZrO_6]^{2-}$ site. Na^+ cations in charge compensating role are less trapped near $[ZrO_6]^{2-}$ site than Na^+ cations near NBOs, which could lower the activation energy for diffusive step and increase mobility of Na^+ in presence of Zr, inducing an enhancement of Na-Ca exchange ratio.

4.2. Validation of matrix diffusion model in the initial composition field

The matrix diffusion model has only been determined from binary exchanges. In geological and industrial domains of interest, multicomponent diffusion often involves more than two composition gradients. To examine the predictive capabilities of our eigenvectors and eigenvalues, additional experiments have been performed for a more complex composition change. The exchange of three oxides, Na_2O, ZrO_2 and Al_2O_3, has been considered between two glasses corresponding to the following equation in weight%. It correspond to an exchange between NA and ZN glasses (Table 1) :

$$4Na_2O \leftrightarrow 2ZrO_2 + 2Al_2O_3 \quad (9)$$

Fig. 9 shows the diffusion exchange between these two glasses at 1200°C for 20 min. The calculations deduced from the diffusion matrix (solid line) are in very good agreement with EPMA experiments (dotted line). This result indicates that the diffusion matrix can be successfully used to predict diffusion exchanges. The prediction error is comparable with fitting errors. Additionally, we also observe that the CaO diffusion profile contains an uphill diffusion appearing with both Al_2O_3 and ZrO_2 having small concentration gradients.

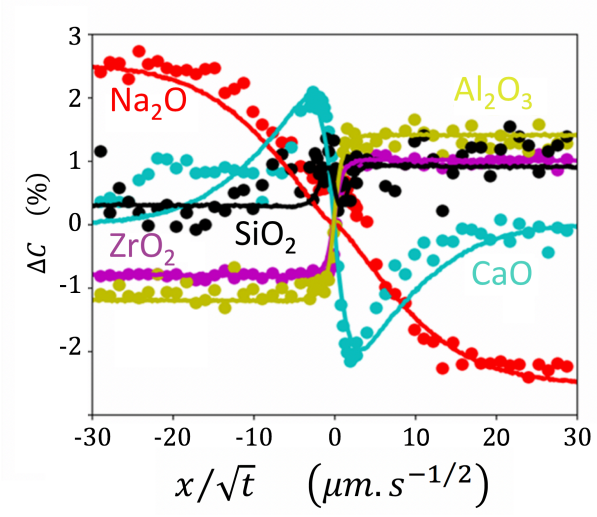

Fig. 9. Diffusion experiment at 1200°C for 20 min between NA and ZN glass. Solid lines represent the predicted diffusion profile when the dots are related to EMPA measurements.

4.3. Diffusion at the crystal-melt interface

The test of the diffusion matrix is also pursued far outside the composition field centered around C_0. Doing that, we consider that a change in fully accounts for diffusivities in the entire NCASZ phase diagram. It is certainly not valid for all compositions but it allows us to get a good estimation of diffusion processes.

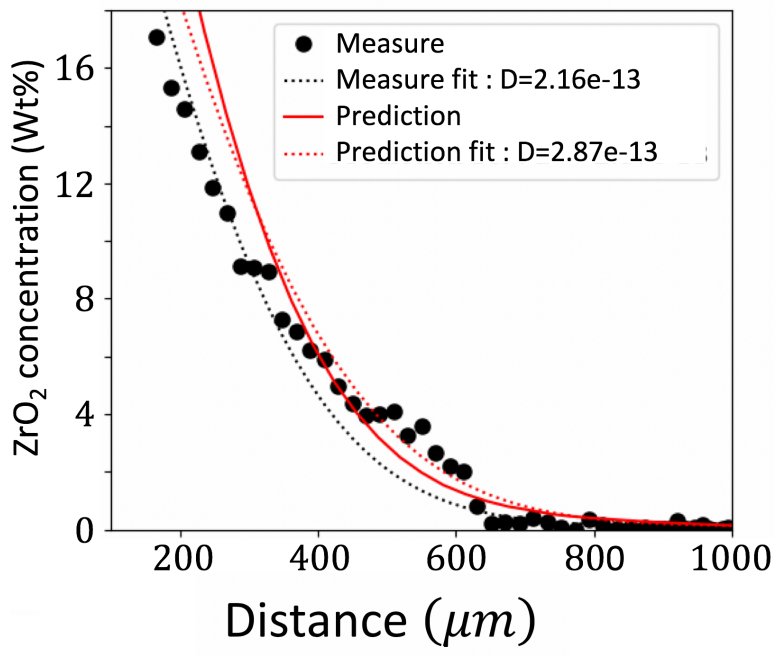

Fig. 10. Diffusion exchange for 40.5 h at 1250°C between $ZrSiO_4$ and G1 (Table 1). The dots represent the EMPA measures when the cyan triangle represents the prediction. The red solid line is the D(Zr) obtained through experimental profile fit with eq. 10.

We were interested in the interaction of crystals with highly viscous melts to reproduce partial dissolution of a mineral. Zircon crystal ($ZrSiO_4$) was investigated and behaves as an infinite reservoir for Zr. The glass in contact with the crystal is a Zr-free NCAS glass of composition G1 (Table 1).

We investigated Zr diffusivity that should control crystal dissolution (and crystal growth) due to the slow Zr diffusion (Bindeman and Melnik, 2016). The diffusion matrix has been used to predict Zr diffusion from zircon crystal towards the G1 glass. A diffusion experiment has also been performed to compare with the matrix predictions. The experiment takes place at 1250°C for 40.5 hours. Composition profiles have been acquired with EPMA. In order to make our results comparable with previous studies, the predicted profiles of ZrO_2 calculated using the diffusion matrix have been fitted with the equation usually used for simple diffusion coefficient determination (Zhang et al., 1989):

$$\frac{C-C_\infty}{C_{zircon}-C_\infty} = erfc\left(\frac{x}{2\sqrt{Dt}} - a\right)\Big/ erfc(-a) \quad (10)$$

and the parameter *a* satisfies the relation:

$$\frac{C_{zircon}-C_\infty}{C_S-C_0} = \sqrt{\pi}ae^{a^2}erfc(-a) \quad (11)$$

C_{zircon} represents the initial concentration in the crystal, C_s corresponds to saturation concentration in glass at the interface ands C_∞ represents the studied element concentration far from the interface.

Fig. 10 presents the diffusion profile of ZrO_2 from zircon towards G1 glass. Both calculations and experiments show similar behaviors: the Zr concentration in the melt is highest at the immediate boundary with the crystal and decreases with increasing distance from the crystal.

The rate of Zr diffusion is described by the apparent diffusion coefficient D(Zr) in the melt that can be calculated using Eq.10 for both the EPMA measurements and the matrix predictions. The D(Zr) obtained from EPMA profile is $2.16*10^{-13}$ m^2s^{-1}. This value can be compared to the one extracted from the matrix predictions: $2.87*10^{-13}$ m^2s^{-1}. Matrix predictions and EPMA experiments differ roughly by a factor of 1.30. The diffusion matrix overestimates the diffusion coefficient. This discrepancy could be partially due to the large viscosity gradient along the diffusion profile that is not taken into account in our diffusion model determined in a very limited composition field. Along a diffusion profile, we expect that there is no change in the exchange reaction (eigenvectors) but the eigenvalues will be affected.

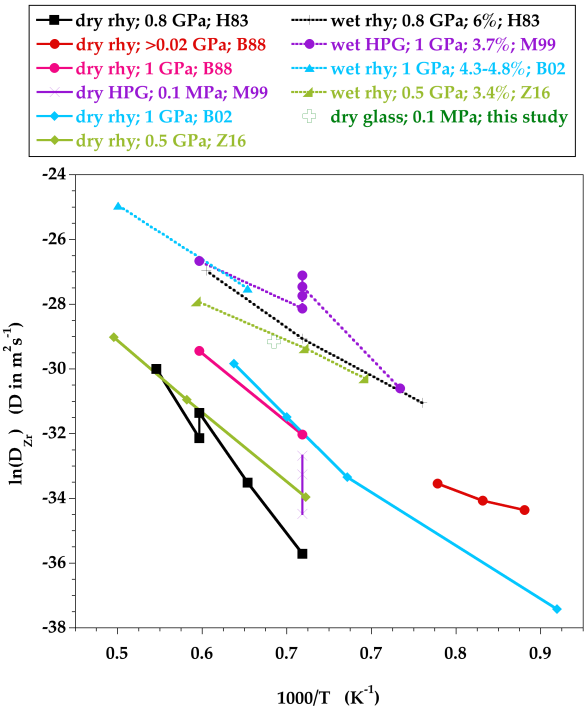

585

586 Fig. 11. Diffusion coefficient of zirconium determined in previous studies for different
587 pressure, water content (dry = solid line) and composition. rhy legend correspond to a rhyolitic
588 melt when HPG is related to basaltic one : HW83(Harrison and Watson 1983); BW88 (Baker
589 and Watson 1988), M99 (Mungall et al 1999); B02 (Baker et al 2002); Z16 (Zhang et al 2016).
590 The current study is also represented.

591

592 We then compare our predicted coefficients with previous studies (Fig. 11). We did not
593 represented our experimental values of D(Zr) because values would be superimposed with
594 predicted ones. Due to the variable compositions, water contents and pressures between our
595 study and the classical geological ones, large differences may occur between the different
596 D(Zr) coefficients. Nevertheless, two groups tend to appear, reflecting mainly the very strong
597 influence of water content on D(Zr). Zr diffusion coefficients are systematically higher for
598 hydrous melts, due to the formation of hydroxyls and non-bridging oxygens resulting in an
599 increase ability to create charge-balanced polyhedra (Freda and Baker, 1998). Surprisingly, the
600 D(Zr) values obtained in the present study are close to those for the hydrous melts group
601 though G1 is a dry glass. However, G1 glass contains a significant Na^+ content contrary to
602 geological glasses in Fig. 11. Those Na^+ cations may play the same role as protons H^+ and
603 increase diffusion in our system, shifting our D(Zr) value from the dry to the hydrated group.
604 A similar mechanism for diffusion, requiring no readjustments of the network topology, has
605 been proposed for water and alkalis by Mungall (Mungall, 2002), pointing to the parallel
606 behavior for Na^+ and H^+ cations.

607 **5. Conclusion**

Using diffusion-couple experiments, the diffusion matrix was determined in a Zr-bearing NCAS glass at 1200°C and 1250°C. The studied system is centered on the composition C_0, 66.4SiO_2-13.3Na_2O-11.95CaO-6.8Al_2O_3-1.55ZrO_2 (NCASZ). A strong coupling between sodium and calcium has been evidenced. A CaO uphill diffusion was showed when ZrO_2 is exchanged with Na_2O. This uphill diffusion was already well known when Al_2O_3 is exchanged with Na_2O. Diffusion matrices have been interpreted using their eigenvalues and eigenvectors. The eigenvectors determined in the present study are remarkably similar to those obtained previously for a similar system without ZrO_2 (Claireaux et al., 2016). On the contrary, eigenvalues are different and reveal higher eigenvalues for NCASZ for at least the two main exchanges, suggesting that a small amount of ZrO_2 in melts tends to increase diffusivity. It is surprising that Zr increases diffusivity and viscosity in melts because those two characteristics show usually opposite trends. Indeed, the diffusion coefficients of network formers calculated from measured viscosity through Eyring relation indicate that adding zirconium should decrease the diffusion coefficients.

Our structural study, coupled with our diffusion one, helped us to understand this phenomenon. Using X-ray absorption spectroscopy (XANES), Zr atoms are determined to be in 6-fold coordinated sites, $[ZrO_6]^{2-}$, in NCASZ glass and these sites are preferentially charge compensated by Na^+. XANES spectra also reveal a competition between $[AlO_4]^-$ and $[ZrO_6]^{2-}$ for charge compensation by Na^+. Raman spectroscopy gave further structural insights, showing that adding ZrO_2 yields a decrease of the number of Q^3(Si) units. This decrease is correlated to the increase of $[ZrO_6]^{2-}$ sites, which indicates a structural change in the role of Na^+. Initially associated with the non-bridging oxygen of SiO_4 polyhedra, Na^+ becomes associated with $[ZrO_6]^{2-}$ sites as charge compensator. The increase of diffusivity may be partially explained by the weak Na-O bond strength when Na^+ atoms charge compensate $[ZrO_6]^{2-}$ polyhedra compare to Na-NBO bond strength. Indeed, activation energy should be lower for Na displacement when it has weaker bond.

Finally we compare the applicability of our diffusion matrix to more general cases, far from the composition field for which the diffusion matrix has been determined. We were able to estimate the diffusion coefficient of zirconium with an error factor of 1.3 which is reasonable considering the large extent of D(Zr) values found in literature.

Acknowledgments

The authors gratefully acknowledge the CAMPARIS microprobe department in Sorbonne University for their experimental help. We acknowledge SOLEIL for beamtime (Proposal 20150961) and for assistance in using LUCIA beamline during the XANES measurements. We also like to thank Olivier Beyssac for his kind help with the Raman spectra acquisition. Finally, we thank Youxue Zhang for his constructive and rigorous reviews of the manuscript.

References

Angeli F., Charpentier T., de Ligny D. and Cailleteauz C. (2010) Boron Speciation in Soda-Lime Borosilicate Glasses Containing Zirconium. *J Am Ceram Soc* **93**, 2693–2704.

649 Baker D. R. and Watson E. B. (1988) Diffusion of major and trace elements in compositionally
650 complex Cl- and F-bearing silicate melts. *J. Non-Cryst. Solids* **102**, 62–70.

651 Behrens H. and Hahn M. (2009) Trace element diffusion and viscous flow in potassium-rich
652 trachytic and phonolitic melts. *Chem. Geol.* **259**, 63–77.

653 Bindeman I. N. and Melnik O. E. (2016) Zircon Survival, Rebirth and Recycling during Crustal
654 Melting, Magma Crystallization, and Mixing Based on Numerical Modelling. *J. Petrol.*
655 **57**, 437–460.

656 Boehnke P., Watson E. B., Trail D., Harrison T. M. and Schmitt A. K. (2013) Zircon saturation
657 re-revisited. *Chem. Geol.* **351**, 324–334.

658 Bouttes D., Lambert O., Claireaux C., Woelffel W., Dalmas D., Gouillart E., Lhuissier P., Salvo
659 L., Boller E. and Vandembroucq D. (2015) Hydrodynamic coarsening in phase-
660 separated silicate melts. *Acta Mater.* **92**, 233–242.

661 Bouvier P., Djurado E., Ritter C., Dianoux A. J. and Lucazeau G. (2001) Low temperature
662 phase transformation of nanocrystalline tetragonal ZrO2 by neutron and Raman
663 scattering studies. *Int. J. Inorg. Mater.* **3**, 647–654.

664 Calas G., Galoisy L., Cormier L., Ferlat G. and Lelong G. (2014) The structural properties of
665 cations in nuclear glasses. *Procedia Mater. Sci.* **7**, 23–31.

666 Chakraborty S., Dingwell D. B. and Rubie D. C. (1995a) Multicomponent diffusion in ternary
667 silicate melts in the system K2O-A12O3-SiO2: II. Mechanisms, systematics, and
668 geological applications. *Geochim. Cosmochim. Acta* **59**, 265–277.

669 Chakraborty S., Dingwell D. B. and Rubie D. C. (1995b) Multicomponent diffusion in ternary
670 silicate melts in the system K2O-Al2O3-SiO2: I. Experimental measurements.
671 *Geochim. Cosmochim. Acta* **59**, 255–264.

672 Chen Y. and Zhang Y. (2008) Olivine dissolution in basaltic melt. *Geochim. Cosmochim. Acta*
673 **72**, 4756–4777.

674 Claireaux C., Chopinet M.-H., Burov E., Gouillart E., Roskosz M. and Toplis M. J. (2016) Atomic
675 mobility in calcium and sodium aluminosilicate melts at 1200 °C. *Geochim.*
676 *Cosmochim. Acta* **192**, 235–247.

677 Claireaux C., Chopinet M.-H., Burov E., Montigaud H., Roskosz M., Toplis M. J. and Gouillart
678 E. (2019) Influence of temperature on multicomponent diffusion in calcium and
679 sodium aluminosilicate melts. *J. Non-Cryst. Solids* **505**, 170–180.

680 Cormier L., Dargaud O., Calas G., Jousseaume C., Papin S., Trcera N. and Cognigni A. (2015) Zr
681 environment and nucleation role in aluminosilicate glasses. *Mater. Chem. Phys.* **152**,
682 41–47.

683 Cormier L., Ghaleb D., Delaye J. M. and Calas G. (2000) Competition for charge compensation
684 in borosilicate glasses: Wide-angle x-ray scattering and molecular dynamics
685 calculations. *Phys. Rev. B* **61**, 14495–14999.

686 Dargaud O., Cormier L., Menguy N., Galoisy L., Calas G., Papin S., Querel G. and Olivi L. (2010)
687 Structural role of Zr4+ as a nucleating agent in a MgO–Al2O3–SiO2 glass-ceramics: A
688 combined XAS and HRTEM approach. *J. Non-Cryst. Solids* **356**, 2928–2934.

689 Dargaud O., Cormier L., Menguy N., Patriarche G. and Calas G. (2011) Mesoscopic scale
690 description of nucleation processes in glasses. *Appl. Phys. Lett.* **99**, 021904.

691 Dimbleby V. and Turner W. E. S. (1926) The relationship between chemical composition and
692 the resistance of glasses to the action of chemical reagents. Part.1. *J Soc Glass*
693 *Technol* **10**, 304–358.

694 Edwards B. R. and Russell J. K. (1996) A review and analysis of silicate mineral dissolution
695 experiments in natural silicate melts. *Chem. Geol.* **130**, 233–245.

696 Eyring H. (1936) Viscosity, Plasticity, and Diffusion as Examples of Absolute Reaction Rates. *J*
697 *Chem Phys* **4**, 283–291.

698 Fluegel A. (2007) Glass viscosity calculation based on a global statistical modelling approach.
699 *Glass Technol-Part A* **48**, 13–30.

700 Freda P. and Baker D. R. (1998) Na-K interdiffusion in alkali feldspar melts. *Geochem.*
701 *Cosmochim. Acta* **62**, 2997–3007.

702 Galoisy L., Pélegrin E., Arrio M.-A., Ildefonse P., Calas G., Ghaleb D., Fillet C. and Pacaud F.
703 (1999) Evidence for 6-Coordinated Zirconium in Inactive Nuclear Waste Glasses. *J.*
704 *Am. Ceram. Soc.* **82**, 2219–2224.

705 Gin S., Abdelouas A., Criscenti L. J., Ebert W. L., Ferrand K., Geisler T., Harrison M. T., Inagaki
706 Y., Mitsui S., Mueller K. T., Marra J. C., Pantano C. G., Pierce E. M., Ryan J. V.,
707 Schofield J. M., Steefel C. I. and Vienna J. D. (2013) An international initiative on long-
708 term behavior of high-level nuclear waste glass. *Mater. Today* **16**, 243–248.

709 Greaves G. N. and Ngai K. L. (1995) Reconciling ionic-transport properties with atomic
710 structure in oxide glasses. *Phys. Rev. B* **52**, 6358–6380.

711 Guo C. and Zhang Y. (2018) Multicomponent diffusion in basaltic melts at 1350 °C. *Geochim.*
712 *Cosmochim. Acta* **228**, 190–204.

713 Guo C. and Zhang Y. (2016) Multicomponent diffusion in silicate melts: SiO2–TiO2–Al2O3–
714 MgO–CaO–Na2O–K2O System. *Geochim. Cosmochim. Acta* **195**, 126–141.

715 Harrison T. M. and Watson E. B. (1983) Kinetics of zircon dissolution and zirconium diffusion
716 in granitic melts of variable water content. *Contrib. Mineral. Petrol.* **84**, 66–72.

717 Heitz J.-L. (1999) Origin of defects related to the corrosion of the refractories in lead crystal
718 glass. *Ceram. Silik.* **43**, 151–155.

719 Howard C. J., Hill R. J. and Reichert B. E. (1988) Structures of ZrO2 polymorphs at room
720 temperature by high-resolution neutron powder diffraction. *Acta Crystallogr. B* **44**,
721 116–120.

Kato K. and Araki N. (1986) The corrosion of zircon and zirconia refractories by molten glasses. *J. Non-Cryst. Solids* **80**, 681–687.

Kress V. C. and Ghiorso M. S. (1993) Multicomponent diffusion in MgO-Al2O3-SiO2 and CaO-MgO-Al2O3-SiO2 melts. *Geochim. Cosmochim. Acta* **57**, 4453–4466.

Larner L. J., Speakman K. and Majumdar A. J. (1976) Chemical interactions between glass fibres and cement. *J. Non-Cryst. Solids* **20**, 43–74.

LaTourrette T., Wasserburg G. J. and Fahey A. J. (1996) Self diffusion of Mg, Ca, Ba, Nd, Yb, Ti, Zr, and U in haplobasaltic melt. *Geochim. Cosmochim. Acta* **60**, 1329–1340.

Lesher C. E. (2010) Self-diffusion in Silicate Melts: Theory, Observations and Applications to Magmatic Systems. *Rev. Mineral. Geochem.* **72**, 269–309.

Liang Y. (2010) Multicomponent Diffusion in Molten Silicates: Theory, Experiments, and Geological Applications. *Rev. Mineral. Geochem.* **72**, 409–446.

Liang Y., Richter F. M., Davis A. M. and Bruce Watson E. (1996a) Diffusion in silicate melts: I. Self diffusion in CaOAl203SiO2 at 1500°C and 1 GPa. *Geochim. Cosmochim. Acta* **60**, 4353–4367.

Liang Y., Richter F. M. and Watson E. B. (1996b) Diffusion in silicate melts: II. Multicomponent diffusion in CaOAl2O3SiO2 at 1500°C and 1 GPa. *Geochim. Cosmochim. Acta* **60**, 5021–5035.

Long D. A. (1977) *Raman spectroscopy*., McGraw-Hill.

Manfredo L. J. and McNally R. N. (1984) Solubility of Refractory Oxides in Soda-Lime Glass. *J. Am. Ceram. Soc.* **67**, C-155-C–158.

Mazurin O. V. and Streltsina M. V. (1972) Determination of tie-line directions in the metastable phase-separation regions of ternary systems. *J Non-Cryst Solids* **11**, 199–218.

McKeown D. A. Muller, I. S. ,. Buechele, A. C. ,. Pegg, I. L. (2000) Local environment of Zn in zirconium borosilicate glasses by X-ray absorption spectroscopy. *J Non-Cryst Solids* **261**, 155–162.

McKeown D. A., Muller I. S., Buechele A. C. and Pegg I. L. (1999) X-ray absorption studies of the local environment of Zr in high-zirconia borosilicate glasses. *J. Non-Cryst. Solids* **258**, 98–109.

McMillan P. and Piriou B. (1982) The structures and vibrational spectra of crystals and glasses in the silica-alumina system. *J. Non-Cryst. Solids* **53**, 279–298.

Mungall J. E. (2002) Empirical models relating viscosity and tracer diffusion in magmatic silicate melts. *Geochim. Cosmochim. Acta* **66**, 125–143.

Mungall J. E., Dingwell D. B. and Chaussidon M. (1999) Chemical diffusivities of 18 trace elements in granitoid melts. *Geochim. Cosmochim. Acta* **63**, 2599–2610.

Mungall J. E., Romano C. and Dingwell D. B. (1998) Multicomponent diffusion in the molten system K2O-Na2O-Al2O3-SiO2-H2O. *Am. Mineral.* **83**, 685–699.

Mysen B. O., Finger L. W., Virgo D. and Seifert F. A. (1982) Curve-fitting of Raman spectra of silicate glasses. *Am. Mineral.* **67**, 686–695.

Neuville D. R., Cormier L. and Massiot D. (2006) Al coordination and speciation in calcium aluminosilicate glasses: effects of composition determined by 27Al MQ-MAS NMR and Raman spectroscopy. *Chem Geol* **229**, 173–185.

Neuville D. R., Cormier L. and Massiot D. (2004) Al environment in tectosilicate and peraluminous glasses: a 27Al MQ-MAS NMR, Raman, and EXAFS investigation. *Geochim Cosmochim Acta* **68**, 5071–5079.

Ni H., Hui H. and Steinle-Neumann G. (2015) Transport properties of silicate melts. *Rev. Geophys.* **53**, 715–744.

Pablo H., Schuller S., Toplis M. J., Gouillart E., Mostefaoui S., Charpentier T. and Roskosz M. (2017) Multicomponent diffusion in sodium borosilicate glasses. *J. Non-Cryst. Solids* **478**, 29–40.

Petrescu S., Constantinescu M., Anghel E. M., Atkinson I., Olteanu M. and Zaharescu M. (2012) Structural and physico-chemical characterization of some soda lime zinc alumino-silicate glasses. *J. Non-Cryst. Solids* **358**, 3280–3288.

Quintas A., Caurant D., Majérus O., Charpentier T. and Dussossoy J. L. (2009) Effect of compositional variations on charge compensation of AlO4 and BO4 entities and on crystallization tendency of a rare-earth-rich aluminoborosilicate glass. *Mater. Res. Bull.* **44**, 1895–1898.

Quintas A., Caurant D., Majérus O., Loiseau P., Charpentier T. and Dussossoy J.-L. (2017) ZrO2 addition in soda-lime aluminoborosilicate glasses containing rare earths: Impact on rare earths environment and crystallization. *J. Alloys Compd.* **719**, 383–391.

Rahimi R. A., Ahmadi A., Kakooei S. and Sadrnezhaad S. K. (2011) Corrosion behavior of ZrO2–SiO2–Al2O3 refractories in lead silicate glass melts. *J. Eur. Ceram. Soc.* **31**, 715–721.

Ravel B. and Newville M. (2005) ATHENA ,ARTEMIS ,HEPHAESTUS : data analysis for X-ray absorption spectroscopy using IFEFFIT. *J. Synchrotron Radiat.* **12**, 537–541.

Richter F. M., Liang Y. and Minarik W. G. (1998) Multicomponent diffusion and convection in molten MgO-Al2O3-SiO2. *Geochim. Cosmochim. Acta* **62**, 1985–1991.

Roskosz M., Toplis M. J. and Richet P. (2006) Kinetic vs. thermodynamic control of crystal nucleation and growth in molten silicates. *J Non-Cryst Solids* **352**, 180–184.

792 Schaller T. Stebbins, J. F. ,. Wilding, M. C. (1999) Cation clustering and formation of free
793 oxide ions in sodium and potassium lantanum silicate glasses: nuclear magnetic
794 resonance and Raman spectroscopic findings. *J Non-Cryst Solids* **243**, 146–157.

795 Simon J. I., Renne P. R. and Mundil R. (2008) Implications of pre-eruptive magmatic histories
796 of zircons for U–Pb geochronology of silicic extrusions. *Earth Planet. Sci. Lett.* **266**,
797 182–194.

798 Sugawara H., Nagata K. and Goto K. S. (1977) Interdiffusivities matrix of CaO-Al2O3-SiO2
799 melt at 1723 K to 1823 K. *Metall. Trans. B* **8**, 605–612.

800 Trial A. F. and Spera F. J. (1994) Measuring the multicomponent diffusion matrix:
801 Experimental design and data analysis for silicate melts. *Geochim. Cosmochim. Acta*
802 **58**, 3769–3783.

803 Valley J. W., Lackey J. S., Cavosie A. J., Clechenko C. C., Spicuzza M. J., Basei M. A. S.,
804 Bindeman I. N., Ferreira V. P., Sial A. N., King E. M., Peck W. H., Sinha A. K. and Wei C.
805 S. (2005) 4.4 billion years of crustal maturation: oxygen isotope ratios of magmatic
806 zircon. *Contrib. Mineral. Petrol.* **150**, 561–580.

807 Wyckoff R. W. G. (1963) *Crystal Structures*. 2nd Ed., Interscience Publishers, New York.

808 Zhang S.-L., Wang X.-N., Li C.-X. and Li C.-J. (2018) Sodium ionic conductivity and stability of
809 amorphous Na2O·2SiO2 added with MxOy (M = Zr, Y, and Sm). *Mater. Des.* **143**, 104–
810 111.

811 Zhang Y., Ni H. and Chen Y. (2010) Diffusion Data in Silicate Melts. *Rev. Mineral. Geochem.*
812 **72**, 311–408.

813 Zhang Y., Walker D. and Lesher C. E. (1989) Diffusive crystal dissolution. *Contrib. Mineral.*
814 *Petrol.* **102**, 492–513.

815 Zhang Y. and Xu Z. (2016) Zircon saturation and Zr diffusion in rhyolitic melts, and zircon
816 growth geospeedometer. *Am. Mineral.* **101**, 1252–1267.

817

818 **SUPPLEMENTARY INFORMATION**

819

820

821 Fig. S1. Viscosity of end-member melts obtained from rotating-cylinder viscometry.
822 Experimental points (symbols) are fitted with a Vogel–Fulcher–Tammann law.
823

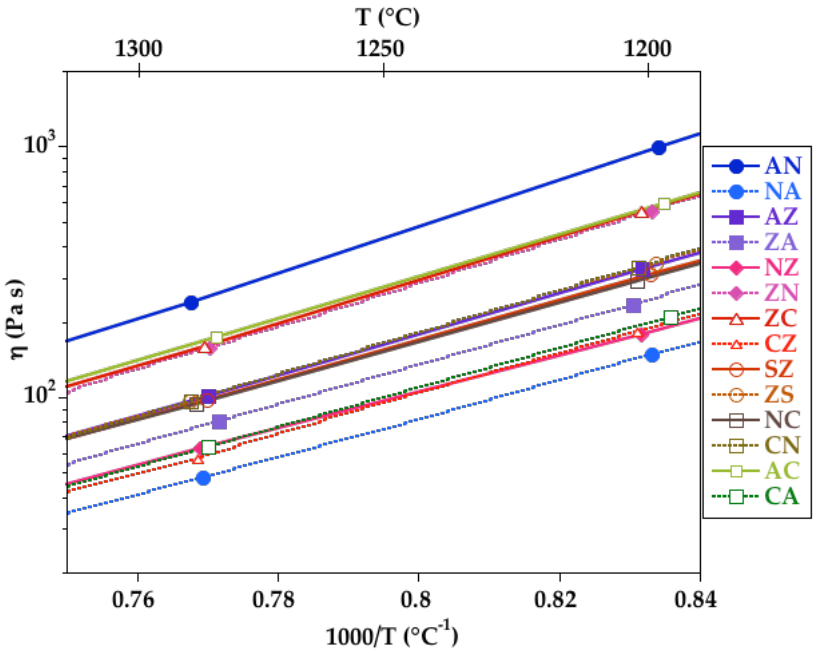
T (°C)
1300
1250
1200
10^3
10^2
η (Pa s)
0.76
0.78
0.8
0.82
0.84
1000/T (°C^{-1})
AN
NA
AZ
ZA
NZ
ZN
ZC
CZ
SZ
ZS
NC
CN
AC
CA

824

825

826

827

828 Table S1. List of experiments and experimental diffusion conditions.

	M_1	M_2	T(°C)	t
Exp 1	AC	CA	1200-1250	20min
Exp 2	NA	AN	1200-1250	20 min
Exp 3	ZA	AZ	1200-1250	20 min
Exp 4	NC	CN	1200-1250	20 min
Exp 5	NZ	ZN	1200-1250	20 min
Exp 6	CZ	ZC	1200-1250	20 min
Exp 7	SZ	ZS	1200-1250	20 min
Exp 8	NA	ZN	1200	20 min
Exp 9	$ZrSiO_4$	G1	1250	40.5 h

829

830 Table S2. Interface (average) compositions of each diffusion couple (weight%).

	Na_2O	CaO	ZrO_2	Al_2O_3	SiO_2
C_0	12.9	10.5	3	10.9	62.50
AC-CA	12.4	10.00	2.65	11.35	64.70
AN-NA	11.85	10.45	2.70	11.8	63.10
AZ-ZA	12.35	9.7	2.55	10.95	61.35
NC-CN	12.35	11.64	2.75	11.65	60.7
NZ-ZN	12.35	9.5	2.70	11.40	63.50
ZC-CZ	12.85	11.25	2.75	11.50	61.90
SZ-ZS	12.05	9.75	2.65	11.20	63.75
Average	12.39	10.35	2.72	11.34	62.69
Standard deviation	0.36	0.77	0.13	0.32	1.33

831

832

833

834

835